Adiabatic and diabatic responses of H2+ to an intense femtosecond laser pulse: Dynamics of the electronic and nuclear wave packet

doi: 10.1063/1.478002

Adiabatic and diabatic responses of H_2^+ to an intense femtosecond laser pulse: Dynamics of the electronic and nuclear wave packet

Isao Kawata, Hirohiko Kono, and Yuichi Fujimura
Department of Chemistry, Graduate School of Science, Tohoku University, Sendai 980-8578, Japan

(Received 11 December 1998; accepted 16 March 1999)

We investigate the quantal dynamics of the electronic and nuclear wave packet of H_2^+ in strong femtosecond pulses ($\geqslant 10^{14}\,W/cm^2$). A highly accurate method which employs a generalized cylindrical coordinate system is developed to solve the time-dependent Schrödinger equation for a realistic three-dimensional (3D) model Hamiltonian of H_2^+. The nuclear motion is restricted to the polarization direction z of the laser electric field $E(t)$. Two electronic coordinates z and ρ and the internuclear distance R are treated quantum mechanically without using the Born-Oppenheimer approximation. As the 3D packet pumped onto $1\sigma_u$ moves toward larger internuclear distances, the response to an intense laser field switches from the adiabatic one to the diabatic one; i.e., electron density transfers from a well associated with a nucleus to the other well every half optical cycle, following which interwell electron transfer is suppressed. As a result, the electron density is asymmetrically distributed between the two wells. Correlations between the electronic and nuclear motions extracted from the dynamics starting from $1\sigma_u$ can be clearly visualized on the time-dependent ''effective'' 2D surface obtained by fixing ρ in the total potential. The 2D potential has an ascending and descending valley along $z=\pm R/2$ which change places with each other every half cycle. In the adiabatic regime, the packet starting from $1\sigma_u$ stays in the ascending valley, which results in the slowdown of dissociative motion. In the diabatic regime, the dissociating packet localized in a valley gains almost no extra kinetic energy because it moves on the descending and ascending valleys alternately. Results of the 3D simulation are also analyzed by using the phase-adiabatic states $|1\rangle$ and $|2\rangle$ that are adiabatically connected with the two states $1\sigma_g$ and $1\sigma_u$ as $E(t)$ changes. The states $|1\rangle$ and $|2\rangle$ are nearly localized in the descending and the ascending valley, respectively. In the intermediate regime, both $|1\rangle$ and $|2\rangle$ are populated because of nonadiabatic transitions. The interference between them can occur not only at adiabatic energy crossing points but also near a local maximum or minimum of $E(t)$. The latter type of interference results in ultrafast interwell electron transfer within a half cycle. By projecting the wave packet onto $|1\rangle$ and $|2\rangle$, we obtain the populations of $|1\rangle$ and $|2\rangle$, P_1 and P_2, which undergo losses due to ionization. The two-state picture is validated by the fact that all the intermediates in other adiabatic states than $|1\rangle$ and $|2\rangle$ are eventually ionized. While $E(t)$ is near a local maximum, P_2 decreases but P_1 is nearly constant. We prove from this type of reduction in P_2 that ionization occurs mainly from the upper state $|2\rangle$ (the ascending well). Ionization is enhanced irrespective of the dissociative motion, whenever P_2 is large and the barriers are low enough for the electron to tunnel from the ascending well. The effects of the packet's width and speed on ionization are discussed. © *1999 American Institute of Physics.* [S0021-9606(99)00822-3]

I. INTRODUCTION

Current laser technology has enabled experimentalists to concentrate radiation energy to very intense levels on time scales of electronic motion. For atoms interacting with intense laser fields, one of the main subjects is dynamics of electrons.[1] Special attention has been paid to new nonlinear optical processes such as above-threshold ionization[2–4] and high-order harmonic generation of emission (HHG).[5–13] In the high-intensity and low-frequency range, the Coulomb potential distorted by the laser electric field forms a ''quasistatic'' barrier through which an electron can tunnel. The rate of tunneling ionization can be calculated by ''quasistatic'' theories.[14–18] Corkum[13] has well explained the mechanism of HHG by assuming that the velocity of the electron after quasistatic tunneling is zero and the evolution of the ejected electron is described by classical mechanics (high-order harmonics is generated when the electron circles back to the vicinity of the nucleus).

For molecules, another kind of internal motion, namely, nuclear motion, is also involved in the dynamics of the system. Recent experiments and theories in a strong laser field case ($>10^{11}\,W/cm^2$) have underscored the combined process of photodissociation and photoionization. It has been experimentally revealed that the kinetic energies of fragments are consistent with Coulomb explosions at specific internuclear distances in the range of 7–10 a.u.[19–24] An explanation for this finding is as follows: ionization rates at the critical internuclear distances exceed those near the equilibrium inter-

nuclear distance and those of dissociative fragments, and ionization to higher-charge states occurs when the nuclei pass through the critical range.[23–27]

The fact that ionization is enhanced at critical internuclear distances suggests that strong correlation between the electronic motion and the nuclear configuration/motion exists in intense laser fields. Although a large number of theoretical studies[24,28–33] have been made on molecular dynamics in laser fields, our knowledge is still limited, especially, as to how an electron (or electrons) and nuclei move in intense laser fields and as to how these two motions are correlated with each other. In a previous paper,[34] we have studied the quantal dynamics of H_2^+ as to how the electronic motion induced by an intense laser pulse ($>10^{14}\,W/cm^2$) affects the nuclear motion. The question to be posed next is how the electronic motion reacts to the initiated nuclear motion. In this paper, by accurately solving the time-dependent Schrödinger equation for a realistic 3D model Hamiltonian of H_2^+, we investigate effects of the nuclear motion on enhanced ionization and on electron transfer between the two wells associated with two nuclei. Although nuclear motion is, in the model, restricted to the polarization direction z of the laser electric field, the electronic coordinates z and ρ (perpendicular to z) and the internuclear distance R are treated quantum mechanically without using the Born-Oppenheimer (B-O) separation. The electronic and nuclear wave packet can be visualized on the time-dependent ''effective'' 2D surface obtained by fixing ρ in the total potential.

The response of the electron to a time-dependent laser electric field is classified into the adiabatic and diabatic regimes. For H_2^+, there are two electronic states $1\sigma_g$ and $1\sigma_u$ which are strongly coupled with each other by radiative interaction. Two ''phase-adiabatic'' states are defined as time-dependent eigenfunctions that are obtained by diagonalizing the electronic Hamiltonian (including the dipole interaction with the classical electric field) in terms of the two B-O electronic wave functions $1\sigma_g$ and $1\sigma_u$. The electronic and nuclear correlation dynamics is analyzed by using the two phase-adiabatic states and nonadiabatic transitions between them. We also examine the mechanism of ionization in an intense field by projecting the wave packet onto the two phase-adiabatic states. The validity of the two-state picture is discussed.

When irradiated by an intense laser pulse, H_2^+ photodissociates as $H_2^+ \rightarrow H^+ + H$ or photoionizes followed by Coulomb explosion as $H_2^+ \rightarrow H^+ + H^+ + e^-$. Fundamental patterns of electronic and nuclear correlation dynamics can be extracted by starting from the excited electronic state $1\sigma_u$. The molecule is assumed to be vertically excited from the vibrational ground state of $1\sigma_g$. In this case, without an intense field, the molecule just dissociates. In this paper, on condition that the packet is initially pumped to $1\sigma_u$, the dissociation and photoionization processes in an intense field and their interplay are discussed. The initial condition of starting from $1\sigma_u$ makes the discussion simpler than the other case of starting from $1\sigma_g$, since the bound component of nuclear motion does not appear in the former case (the gained kinetic energy of dissociative motion is large).

The rest of this paper is organized as follows. In Sec. II, we generalize the method developed for the H atom[35] to solve the time-dependent Schrödinger equation for a 3D model of H_2^+ (only the internuclear distance is considered as a nuclear coordinate) and to investigate the electronic and nuclear full dynamics in currently available ultraintense, ultrashort laser pulses. In Sec. III, the coupled equations for the two phase-adiabatic states are derived to analyze the full 3D dynamics. Adiabaticity and nonadiabatic transitions are outlined. In Sec. IV, results of the 3D simulation are presented. Electronic and nuclear motions caused by an intense field are analyzed using the time-dependent surface composed of the Coulomb potentials and the dipole interaction, as well as using the two phase-adiabatic states (and nonadiabatic transitions). Finally, in Sec. V, concluding remarks are given with a brief summary of the present work.

II. A NUMERICAL METHOD FOR A 3D H_2^+ SYSTEM

In this work, we use the 3D model employed in Ref. 24. In the model, the following assumptions are made: the applied laser fields are linearly polarized along the z-axis; the nuclear motion is restricted to the polarization direction of the laser electric field. The electron moves in three dimensions. Because of the cylindrical symmetry of the model, the z-component of the electronic angular momentum, $m\hbar$, is conserved; the electronic degrees of freedom to be considered are two cylindrical coordinates z and ρ. Here, ρ and z are measured with respect to the center of mass of the two nuclei, $\mathbf{r}_{cn}$.

The time-dependent Schrödinger equation of this three-body system is written in the following form after separation of the center-of-mass coordinate, $\mathbf{r}_c$ (throughout this paper atomic units are used),

$$
\begin{aligned}
i\frac{\partial}{\partial t}\phi(\rho,z,R) &= \left\{ -\frac{1}{m_p}\frac{\partial^2}{\partial R^2} - \frac{1}{2\mu}\left(\frac{\partial^2}{\partial \rho^2} + \frac{1}{\rho}\frac{\partial}{\partial \rho} + \frac{\partial^2}{\partial z^2} \right) \right. \\
&\quad \left. + \frac{m^2}{2\rho^2} + V(\rho,z,R) + V_E(z,t) \right\} \phi(\rho,z,R), \qquad (2.1)
\end{aligned}
$$

where R is the internuclear distance, m_e and m_p are electron and nuclear masses, and $\mu = 2m_p m_e/(2m_p + m_e)$. The potential $V(\rho,z,R)$ is the sum of the Coulomb interactions

$$
V(\rho,z,R) = \frac{1}{R} - \frac{1}{\sqrt{\rho^2 + (z - R/2)^2}} - \frac{1}{\sqrt{\rho^2 + (z + R/2)^2}}, \qquad (2.2)
$$

and the dipole interaction $V_E(z,t)$ between the molecule and the electric field $E(t)$ of a laser pulse,[36]

$$
V_E(z,t) = z\left(1 + \frac{m_e}{2m_p + m_e} \right) E(t). \qquad (2.3)
$$

The dipole moment is given by $(z_a - z_c) + (z_b - z_c) - (z_e - z_c) = -2(z_c - z_{cn}) - [z_e - z_{cn} - (z_c - z_{cn})]$, where z_a, z_b, and z_e represent the coordinates of the two nuclei and the electron, respectively, all measured with respect to the laboratory system (the subscript c stands for the center-of-mass

coordinate and *cn* stands for the center of mass of the two nuclei). Using the difference $z_c - z_{cn} = z m_e/(2m_p + m_e)$, we obtain Eq. (2.3).

We spatially discretize the Hamiltonian to solve the time-dependent Schrödinger Eq. (2.1). The finite difference method is chosen to evaluate the differential operators contained in the Hamiltonian. It should, however, be noted that the Coulomb potential is characterized by its long range and its singularity at the origin. The grid boundary in coordinate space must be chosen to be far from the origin to accommodate the wave function and the grid spacings must be small to generate high momentum components near the origin. To overcome these obstacles, we present a new method where the finite difference method is effectively used. The basic idea for the new method is developed in a previous paper.[35]

For the cylindrical coordinate system, the finite difference method does not give sufficient accuracy. The coordinate system to be employed must satisfy the following two requirements: (i) the differential operators can be well evaluated by the finite difference method even near the Coulomb singular points (the positions of nuclei); (ii) the equal spacings in the new coordinates correspond to grid spacings in the cylindrical coordinates that are small near the nuclei and are large at larger distances therefrom. Variable transformations (mapping procedures) have been used to reduce the number of representation points for electronic structure calculations.[37–39] We propose the generalized cylindrical coordinate system as

$$\rho = f(\xi); \quad z = g(\zeta), \tag{2.4}$$

where $f(\xi)$ and $g(\zeta)$ are functions for variable transformation to fulfill the above two requirements.

The function $\phi(\rho,z,R)$ is normalized as

$$\int_0^\infty dR \int_0^\infty d\rho \int_{-\infty}^\infty dz \rho |\phi(\rho,z,R)|^2 = 1. \tag{2.5}$$

When the finite difference method is used, it is generally difficult to conserve the norm of the wave function. It has been known that to conserve the norm numerically the following normalization condition should be imposed on the transformed wave function $\psi(\xi,\zeta,R)$,[35]

$$\int_0^\infty dR \int_0^\infty d\xi \int_{-\infty}^\infty d\zeta |\psi(\xi,\zeta,R)|^2 = 1. \tag{2.6}$$

Note that the volume element for normalization is $dR d\xi d\zeta$, not like $\xi dR d\xi d\zeta$.

The transformed wave function that satisfies the normalization condition Eq. (2.6) is uniquely determined as

$$\psi(\xi,\zeta,R) = \sqrt{f(\xi) f'(\xi) g'(\zeta)}\, \phi(f(\xi), g(\zeta), R), \tag{2.7}$$

where the function with a prime denotes the derivative with respect to its argument. Inserting Eq. (2.7) into Eq. (2.1), one obtains the following equation:

$$i \frac{\partial \psi(\xi,\zeta,R)}{\partial t} = \hat{H} \psi(\xi,\zeta,R), \tag{2.8}$$

where the transformed Hamiltonian $\hat{H}$ is given by

$$\hat{H} = K_R + K_\xi + K_\zeta + \frac{m^2}{2\rho^2} + V + V_E. \tag{2.9}$$

The kinetic energy parts with respect to coordinates R, ξ, and ζ, i.e., K_R, K_ξ, and K_ζ are expressed as

$$K_R = -\frac{1}{m_p} \frac{\partial^2}{\partial R^2}, \tag{2.10a}$$

$$K_\xi = -\frac{1}{2\mu f'^2(\xi)} \left\{ \frac{\partial^2}{\partial \xi^2} - \frac{2 f''(\xi)}{f'(\xi)} \frac{\partial}{\partial \xi} + \frac{1}{2 f'^2(\xi)} \times \left[\frac{5}{2} f''^2(\xi) - f'(\xi) f'''(\xi) \right] \right\} - \frac{1}{8\mu f^2(\xi)}, \tag{2.10b}$$

and

$$K_\zeta = -\frac{1}{4\mu} \left[\frac{1}{g'^2(\zeta)} \frac{\partial^2}{\partial \zeta^2} + \frac{\partial^2}{\partial \zeta^2} \frac{1}{g'^2(\zeta)} \right] + \frac{1}{4\mu g'^4(\zeta)} \left[\frac{7}{2} g''^2(\zeta) - g'(\zeta) g'''(\zeta) \right]. \tag{2.10c}$$

The differential operators in Eqs. (2.10) are evaluated using five-point finite difference formulas.

We are now in a position to determine f and g explicitly. To avoid the numerical difficulties concerning the Coulomb singularity, the transformed wave function ψ must be zero at the singular points. This requirement, referred to as (iii), means that the prefactor $\sqrt{f f' g'}$ of the transformed wave function in Eq. (2.7) must be zero at the nuclei. Poor performance of the cylindrical coordinate system originates from the fact that the requirement (i) is not satisfied. For the cylindrical coordinate system, the transformed wave function is not analytic around the singular points because $\sqrt{f f' g'} \approx \sqrt{\rho}$.

To fulfill the three requirements (i)–(iii), we choose in this paper the following variable transformations:

$$f(\xi) = \xi \sqrt{\frac{\xi}{\xi + \alpha}}, \tag{2.11a}$$

$$g(\zeta) = \zeta, \tag{2.11b}$$

where the parameter α is a width in ρ where the potential V is relatively deep. We choose $\Delta\xi = 0.16$, $\Delta\xi = 0.18$, $\Delta R = 0.05$, and $\alpha = 28.3$. The functions in Eqs. (2.11) are not unique. In Ref. 39, the representation efficiency is optimized such that the wasted classical phase space area is minimal (the method is applied to the H_2^+ eigenvalue problem). Whenever more efficient transformations are found, one can replace Eqs. (2.11) with them.

Chelkowski *et al.*[24] have solved Eq. (2.1) with the help of the Bessel–Fourier expansion in the ρ variable. This allows one to eliminate the singularities in the Laplacian and in the potential and to use a split operator propagation method together with fast Fourier transform in z and R. Here, to evolve the wave function according to Eq. (2.8), we employ the alternating-direction implicit (ADI) method,[40] which is adaptable to variable transformations. Among various propagation methods, the ADI method is found to be the

most accurate for steep attractive potentials, at least for the 1D Coulomb potential.[35] A summary of the ADI method is given in the Appendix.

III. TWO PHASE-ADIABATIC STATES

For H_2^+, there are two charge resonance states $1\sigma_g$ and $1\sigma_u$ which are strongly coupled with each other by radiative interaction. It is justified to represent the dynamics of the system in terms of the states $1\sigma_g$ and $1\sigma_u$. The two-state model cannot directly take into account the ionization process but helps to understand the dissociation and photoionization processes.

We start with diagonalizing the electronic part including the radiative interaction,

$$\hat{H}_{el}(t)=-\frac{1}{2\mu}\left(\frac{\partial^2}{\partial\rho^2}+\frac{1}{\rho}\frac{\partial}{\partial\rho}+\frac{\partial^2}{\partial z^2}\right)+\frac{m^2}{2\rho^2}+V(\rho,z,R)+V_E(z,t), \tag{3.1}$$

in terms of the two B-O electronic wave functions $|1\sigma_g\rangle$ and $|1\sigma_u\rangle$ (abbreviated as $|g\rangle$ and $|u\rangle$). The time t and R are treated as adiabatic parameters. The resulting eigenfunctions are given by

$$\begin{aligned}|1\rangle&=\cos\theta|g\rangle-\sin\theta|u\rangle,\\ |2\rangle&=\cos\theta|u\rangle+\sin\theta|g\rangle,\end{aligned} \tag{3.2}$$

where

$$\theta=\frac{1}{2}\arctan\left[\frac{2\langle g|z|u\rangle E(t)}{\Delta E_{ug}(R)}\right], \tag{3.3}$$

with the B-O energy separation $\Delta E_{ug}(R)=E_u(R)-E_g(R)$. The eigenvalues are

$$E_{1,2}(R,t)=\tfrac{1}{2}[E_g(R)+E_u(R)\mp\sqrt{\Delta E_{ug}^2+4|\langle g|z|u\rangle E(t)|^2}]. \tag{3.4}$$

To emphasize the adiabaticity of $|1\rangle$ and $|2\rangle$ with respect to the phase of $E(t)$, we call them ''phase-adiabatic'' states.[41] For H_2^+, the transition moment $\langle g|z|u\rangle$ approaches $R/2$ as R increases.[42]

Using the two phase-adiabatic states, the total wave function is expressed as

$$|\psi\rangle=\chi_1(R)|1\rangle+\chi_2(R)|2\rangle, \tag{3.5}$$

where χ_1 and χ_2 are the nuclear wave functions associated with $|1\rangle$ and $|2\rangle$. Inserting Eq. (3.5) into the time-dependent Schrödinger equation for the Hamiltonian (3.1), we obtain the following coupled equations,

$$\frac{\partial}{\partial t}\chi_1(R)=-i\left[-\frac{1}{m_p}\frac{\partial^2}{\partial R^2}+E_1(R,t)+\frac{1}{m_p}\left(\frac{\partial\theta}{\partial R}\right)^2\right]\times\chi_1(R)-\Lambda(R,t)\chi_2(R), \tag{3.6a}$$

$$\frac{\partial}{\partial t}\chi_2(R)=-i\left[-\frac{1}{m_p}\frac{\partial^2}{\partial R^2}+E_2(R,t)+\frac{1}{m_p}\left(\frac{\partial\theta}{\partial R}\right)^2\right]\times\chi_2(R)+\Lambda(R,t)\chi_1(R), \tag{3.6b}$$

where the laser-induced nonadiabatic coupling is

$$\Lambda(R,t)=\frac{\partial\theta}{\partial t}-\frac{2i}{m_p}\frac{\partial\theta}{\partial R}\frac{\partial}{\partial R}-\frac{i}{m_p}\frac{\partial^2\theta}{\partial R^2}. \tag{3.7}$$

Here the small nonadiabatic coupling terms $\langle g|\partial^2/\partial R^2|g\rangle/m_p$ and $\langle u|\partial^2/\partial R^2|u\rangle/m_p$ are ignored. The term $\partial\theta/\partial t$ is the nonadiabatic coupling due to the change in the electric field, and the other coupling terms in $\Lambda(R,t)$ are due to the joint effect of the electric field and the nuclear motion. Thachuk *et al.*[43] have developed a semiclassical formalism for treating time-dependent Hamiltonians (nuclei are propagated classically on the surfaces) and applied it to the dissociation of diatomic ions. They have derived the nonadiabatic couplings $\partial\theta/\partial t$ and $v\,\partial\theta/\partial R$, where v is the relative nuclear velocity. These two terms correspond to the first and second terms in Eq. (3.7). For homonuclear ions, $\partial\theta/\partial t$ is much larger than $v\,\partial\theta/\partial R$,[43] except when $\Delta E_{ug}\gg\langle g|z|u\rangle\times$(pulse envelope).

Using the two localized states $|R\rangle=(|g\rangle+|u\rangle)/\sqrt{2}$ and $|L\rangle=(|g\rangle-|u\rangle)/\sqrt{2}$, the populations in the right and left wells associated with two nuclei, P_R and P_L, are expressed as follows:

$$P_R(R)=\cos^2\left(\theta+\frac{\pi}{4}\right)|\chi_1(R)|^2+\sin^2\left(\theta+\frac{\pi}{4}\right)|\chi_2(R)|^2+\mathrm{Re}[\cos 2\theta\chi_1^*(R)\chi_2(R)], \tag{3.8a}$$

$$P_L(R)=\sin^2\left(\theta+\frac{\pi}{4}\right)|\chi_1(R)|^2+\cos^2\left(\theta+\frac{\pi}{4}\right)|\chi_2(R)|^2-\mathrm{Re}[\cos 2\theta\chi_1^*(R)\chi_2(R)]. \tag{3.8b}$$

The third term in both equations represents the interference between $|1\rangle$ and $|2\rangle$.

The solution of Eq. (3.6) can be classified by using the following quantity:[44,45]

$$\delta=\left|\frac{\Delta E_{ug}^2(R)}{\langle g|z|u\rangle\varepsilon(t)\omega}\right|, \tag{3.9}$$

where ω is the laser frequency. The adiabatic energies, $E_1(R,t)$ and $E_2(R,t)$, come close to each other when $E(t)=0$, e.g., at $t=n\pi/\omega$ $(n=1,2,...)$ for the electric field $E(t)$ that changes as $\sin(\omega t)$. On condition that the two adiabatic (or diabatic) states do not interfere with each other, the adiabatic and nonadiabatic transition probabilities at each crossing point are well described by the Landau–Zener formulas,[44–46] $P_{\mathrm{ad}}=1-\exp(-\pi\delta/4)$ and $P_{\mathrm{nonad}}=\exp(-\pi\delta/4)$, respectively. For $\delta\gg1$, $P_{\mathrm{ad}}\cong1$, the phase-adiabatic picture of electronic and nuclear dynamics works well. For $\delta\ll1$, the main route is the nonadiabatic channel. As the field changes more slowly, δ becomes larger.

IV. RESULTS AND DISCUSSION

In this section, correlations between the electronic and dissociative motions are extracted from the dynamics starting from $1\sigma_u$. Analyses by the two-state model are presented together with results of the 3D packet simulation. We demonstrate how useful the two-state model is for interpreting

both the dissociation and photoionization processes in intense fields. The procedure taken in the 3D simulation is as follows.

First, the molecule in the ground state $1\sigma_g$ (of the vibrational quantum number $v=0$) is excited onto $1\sigma_u$ by a weak ultrashort pump laser. The pump pulse duration is $T_P=100(2.5\,\mathrm{fs})$ and the frequency is $\omega_P=0.43(105\,\mathrm{nm})$, which corresponds to the energy gap between $1\sigma_g$ and $1\sigma_u$ at $R=2.0$ ($\sim$equilibrium internuclear distance in $1\sigma_g$). The exact ground state of the 3D full system is calculated by operating an energy filter on an approximate ground state to eliminate the excited components.[47] At the end of the pump process the electronically excited component of the packet is normalized to unity.

Second, we apply an intense pulse to the normalized packet on $1\sigma_u$ (we call this pulse the ''second'' pulse). The second pulse is turned on at the end of the pump pulse ($t=0$). In this paper, the electric field of the second pulse is assumed to have the form

$$E(t)=\varepsilon(t)\sin\omega t, \tag{4.1}$$

where $\varepsilon(t)$ is the slowly varying envelope function and ω is the frequency. We use the following envelope function,

$$\varepsilon(t)=\varepsilon_0\sin(\pi t/T) \quad \text{for } 0\leqslant t\leqslant T;$$
$$\text{otherwise } \varepsilon(t)=0, \tag{4.2}$$

where T is the pulse duration and ε_0 is the peak strength. We adopt the following values for the second pulse: $\omega=0.0515(884\,\mathrm{nm})$, $\varepsilon_0=0.096(3.2\times10^{14}\,\mathrm{W/cm^2})$ and $T=400(10\,\mathrm{fs})$. The molecule can be ionized by the second pulse. To eliminate the outgoing component we set absorbing boundaries for the electronic coordinates ρ and z.[48] The ionization probability is calculated by subtracting the remaining norm from the initial norm.

A. Overview of dissociative ionization

Once ionization starts, in general, the packet spreads not only along the polarization direction z but also along the transverse direction ρ. For an intense field like the second pulse, the spread along z is, however, much wider than the transverse one. The key to understanding correlations between the electronic and nuclear motions is hence reduced to the following probability:

$$P(z,R)=\int|\phi(\rho,z,R)|^2\rho d\rho. \tag{4.3}$$

Two snapshots of the probability at $t=0$ (just after the pump pulse has fully decayed) and $t=224$ are illustrated in Figs. 1(a) and 1(b), respectively. The second pulse is applied [$E(t)=-0.0805$ at $t=224$.]

As shown in Fig. 1(a), the probability at $t=0$ is split into the regions around the two nuclei at $z=\pm R_e/2$, where R_e is the equilibrium internuclear distance in $1\sigma_g$. We have confirmed that the packet prepared by the pump pulse is electronically $1\sigma_u$. Since the packet is on the dissociative $1\sigma_u$ potential, the packet moves toward larger internuclear distances as time passes. As shown in Fig. 1(b), the two peaks which are bound to the two nuclei move along $\langle z\rangle=\pm\langle R\rangle/2$. Figure 1(b) also shows the characteristic of photoionization; the second pulse spreads the packet along z. The direction of the ionization flux depends on the phase (positive or negative) of the electric field at the moment.

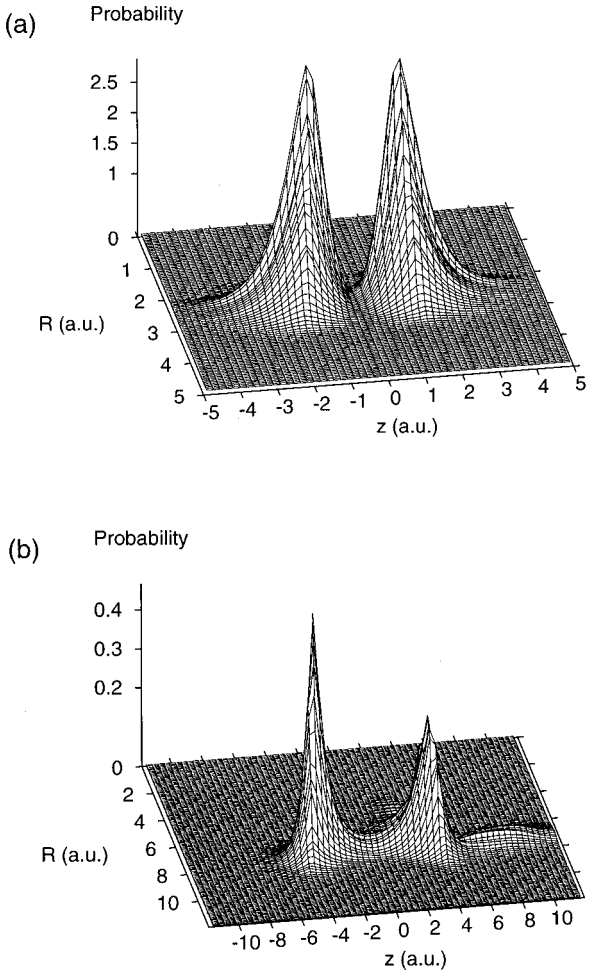

FIG. 1. Characteristic features of dissociative ionization in the 3D simulation. Snapshots of $\int|\phi(\rho,z,R)|^2\rho d\rho$ are taken at (a) $t=0$ and (b) $t=224$. The second pulse is turned on at $t=0$ just after the pump from $1\sigma_g$ to $1\sigma_u$. Comparing the two figures, one finds that the two peaks which are bound to the two nuclei in the dissociation channel $H+H^+$ move along $z=\pm R/2$. In Fig. 1(b), an ionizing component, which protrudes from $z\approx5$ toward larger z, is observed. When the field strength $E(t)<0$, the electron is ejected from the molecule toward positive z. Part of the ejected component circles back to $H_2^{+\,+}$.

The present ionization process falls under the category of tunneling ionization or barrier suppression ionization. The potential distorted by the laser electric field forms a ''quasistatic'' barrier through which the electron can tunnel. Suppose that $E(t)=-0.096$. Cross sections of the instantaneous potential $V(\rho,z,R)+zE(t)$ at four internuclear distances $R=2$, 4, 7, and 14 are plotted in Fig. 2. The transverse coordinate ρ is fixed at 0. Along the polarization axis z, the instantaneous potential has an inner and an outer barrier. Since the barrier heights are the lowest at $\rho=0$, the potential at $\rho=0$ illustrates the main route to ionization. (We fix ρ when the 3D potential is mapped onto 2D or 1D space but never fix ρ in calculating the wave packet dynamics.) When $E(t)<0$, the outer barrier is on the positive-z side. The electric field lowers the barrier(s) for ionization. Tunneling ioniza-

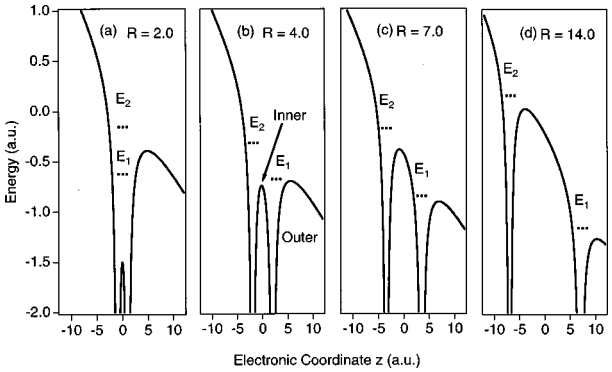

FIG. 2. 1D effective potentials of H_2^+ in an intense field at four internuclear distances $R=2$, 4, 7, and 14. The instantaneous field strength is taken as $E(t)=-0.096$ and ρ is fixed at 0. The total potential is the sum of Eqs. (2.2) and (2.3). Because of its double-well structure at zero field, the distorted potential has an inner and an outer barrier. The energy levels E_1 and E_2 of the two phase-adiabatic states $|1\rangle$ and $|2\rangle$ are given by Eq. (3.4). The gap between E_2 and the maximum of the inner and outer barriers is the largest at $R\approx 4.2$.

tion occurs if the electron has enough time to penetrate the barrier(s) before the phase of the field changes (the process is called ''barrier suppression ionization'' when the barrier is lowered below the energy of the packet). Favorable to tunneling ionization is the condition that the electric field is stronger and its period is longer. The case is classified by the Keldysh parameter $\gamma=\omega\sqrt{2I_p}/\varepsilon_0$,[14–17] where I_p is the ionization potential. The quasistatic tunneling condition is given by the inequality $\gamma<1$. The ordinary multiphoton ionization process is regarded as the opposite case $\gamma>1$.

B. Interwell electron transfer

Besides the ionization process, another type of electronic motion is observed, namely the electron transfer between the two nuclei. As known from Fig. 2, each nucleus works as a potential well for the electron. Electron density can be transferred from well to well by an electric field. We present an example of the electron transfer between the two wells. To focus on the interwell transition, we fix the internuclear distance at $R=4$. We take $1\sigma_u$ as the initial state. The applied pulse is the same as the second pulse used in Fig. 1. Snapshots of the packet at $t=31$ and 92 (a half cycle later) are shown in Figs. 3(a) and 3(b). The unequal electron distribution between the two wells in Fig. 3(a) results from the motion that electron density transfers from the left well at $z=-R/2$ to the right well. The energies of the right and left wells are shifted, respectively, by $\pm RE(t)/2$ because of the dipole interaction term Eq. (2.3). At $t=31$, $E(t)>0$ the ascending well is the right one and the descending well is the left one. The ascending and descending wells change places with each other every half cycle. The electron motion in Fig. 3 means that a part of the electron density is transferred from the descending well to the ascending well (although the force due to the electric field is opposite).

Using the parameter δ already defined in Sec. III, the electronic motion with respect to the change in the electric field can be classified into the adiabatic or diabatic regime according to whether $\delta\gg 1$ or $\delta\ll 1$. At small internuclear

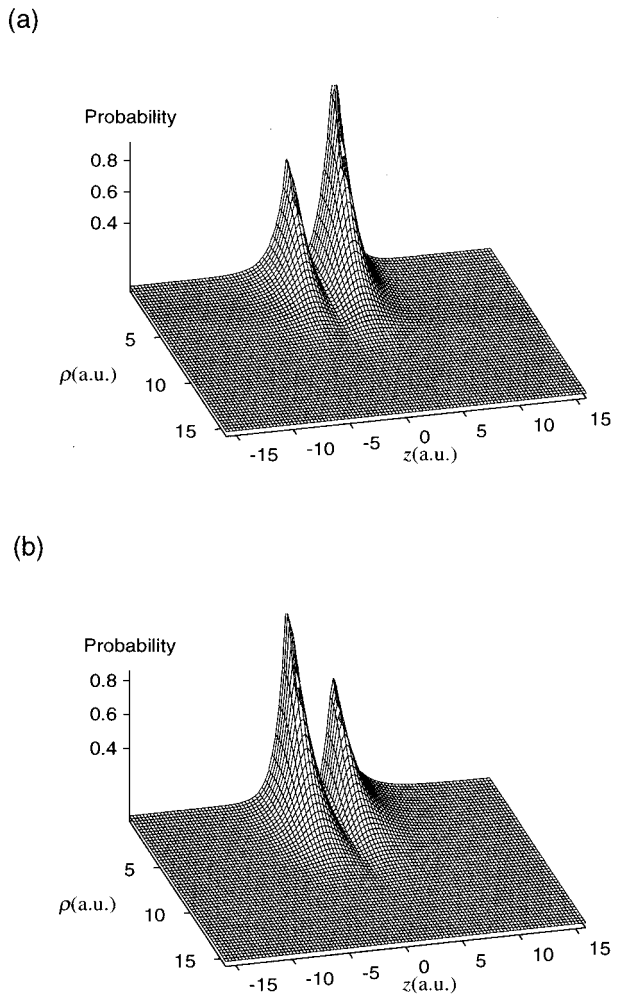

FIG. 3. Interwell electron transfer when the internuclear distance is frozen at $R=4.0$. Snapshots of the probability of the 2D packet are taken at (a) $t=31$ and (b) at $t=92$. The field strength $E(t)$ is 0.023 at $t=31$ and -0.063 at $t=92$. The initial state is $1\sigma_u$. The parameters for the second pulse are the same as used in Fig. 1.

distances, the energy difference ΔE_{ug} is large and the transition moment $\langle g|z|u\rangle$ is relatively small: one can expect that $\delta\gg 1$. Since $\Delta E_{ug}=0.099$ and $\langle g|z|u\rangle=1.8$ at $R=4$, $\delta>1.6$ in the first optical cycle. The case shown in Fig. 3 is nearly adiabatic. According to the adiabatic theorem,[49] if $\delta\gg 1$, the time development of the excited state $1\sigma_u$ is given by the upper phase-adiabatic state $|2\rangle$. Staying in $|2\rangle$ means that the ascending well is more populated as in Fig. 3. If the molecule is initially in the ground state $1\sigma_g$ and the case is adiabatic, electron density transfers from the ascending well to the descending one.

At larger internuclear distances, the transition between the two wells is suppressed. In the diabatic regime, the transition rate for interwell tunneling is given by the well-known form $\Delta E_{ug}J_0[2\langle g|z|u\rangle\varepsilon(t)/\omega]$,[44,50–52] where J_0 is the zeroth order Bessel function. Interwell tunneling is further suppressed with increasing field strength. There also exist specific conditions for the Bessel function to be zero. For the zeros of the Bessel function, interwell transition is inhibited. The coherent destruction of tunneling[50–52] is due to interfer-

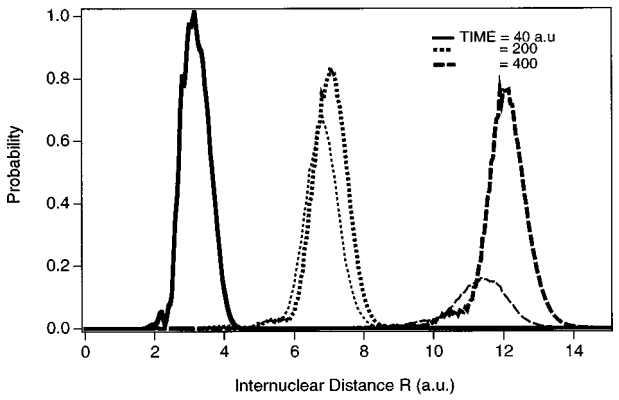

FIG. 4. Probability of finding the molecule at R in the 3D simulation. The bold lines show snapshots under no electric field and the thin ones show those under the intense second pulse. The difference between the two peak positions at $t=400$ indicates the slowdown of dissociative motion by the second pulse.

ence between the two adiabatic (or diabatic) components at periodic crossing points $t_n = n\pi/\omega$ $(n=1,2,...)$.[44]

C. Slowdown of dissociative motion as a result of electronic and nuclear correlation dynamics

In the above subsection, the interwell transition is illustrated but R is fixed. To examine the effect of the interwell transition on the dissociative dynamics, we go back to the 3D simulation. The time-dependent probability of finding the molecule at R,

$$P(R,t) = \int\int |\phi(\rho,z,R)|^2 \rho d\rho dz, \tag{4.4}$$

is presented in Fig. 4. The time is measured from the end of the pump pulse. The thin lines show snapshots of the nuclear motion under the second pulse and the bold ones show those when the second pulse is not applied. Because of ionization, the integrated probability $\int P(R,t)dR$ is smaller in the former case than that in the latter case. It follows from this figure that the dissociative motion is slowed down by the intense laser field. The average kinetic energy of the dissociation products is 4.0 eV without a field and it is reduced to 3.2 eV by the second pulse. For the two cases, the quantum-mechanical average of R is plotted in Fig. 5 as a function of time. The solid line represents the average under the second pulse and the broken line represents the average when the second pulse is not applied.

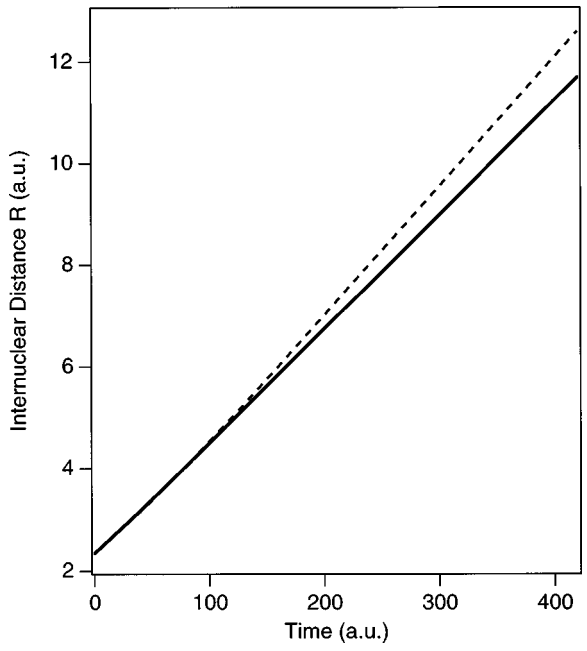

FIG. 5. Quantum-mechanical averages of the internuclear distance in the 3D simulation. The solid line represents the average under the second pulse and the broken line represents the average when the second pulse is not applied.

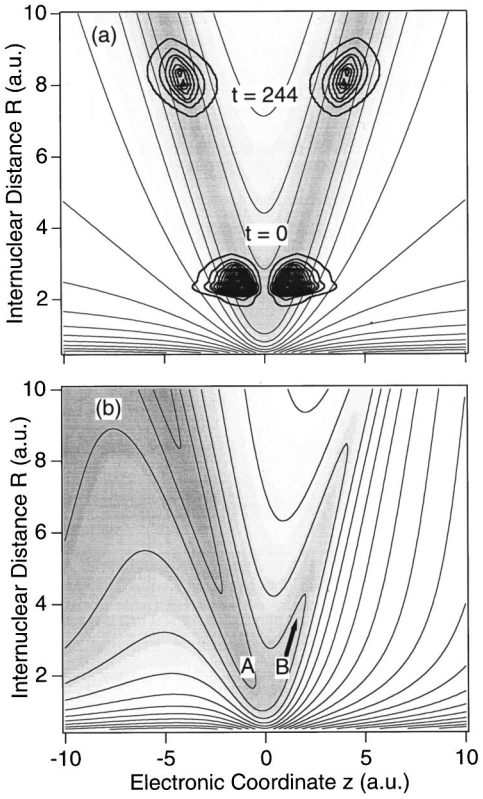

FIG. 6. Time-dependent H_2^+ potential as a function of two variables z and $R(\rho=1.0)$ for (a) zero electric field and (b) a positive electric field $[E(t)=0.09]$. The potential energy is lower in the shaded area. Without the second pulse, the probability of Eq. (4.3) for the packet pumped onto $1\sigma_g$ moves as shown by bold lines in Fig. 6(a).

As mentioned in Sec. IV A, the electronic motion in the intense field is characterized by the 1D motion along the polarization direction z. The ρ-fixed model is known to reproduce quantitative features of the dynamics of the H_2^+ in an intense field.[33] In Ref. 33, the value of ρ is fixed at 1.0; the shapes of the $1\sigma_g$ and $1\sigma_u$ surfaces calculated in the ρ-fixed model are similar to those in the 3D model. The key to illustrate the slowdown of dissociative motion can be given by the time-dependent potential of two variables R and z. Contour maps for the 2D potential are shown in Fig. 6 $(\rho=1.0)$. When the second pulse is not applied [Fig. 6(a)], the packet pumped onto $1\sigma_u$ stays in the two valleys along $z \approx \pm R/2$, moving toward larger R. When the field is applied, as shown in Fig. 6(b), the bottoms of the right and left valleys are shifted by $\pm RE(t)/2$. The ascending (descending)

valley is the sequence of ascending (descending) wells at different R.

During the first half optical cycle $[E(t)>0]$, the greater part of density moves from the descending well to the ascending one [e.g., from A to B in Fig. 6(b)] because at $t=0$ the molecule is in $1\sigma_u$. The component of the wave packet in the right valley starts moving along the ascending valley as denoted by the arrow in Fig. 6(b). In consequence, the dissociative motion is blocked by the upward slope. In the second half cycle $[E(t)<0]$, the packet moves to the left (ascending) well: the motion is again blocked. As a result, during the first cycle, the dissociative motion of the packet is slowed down by the field. In the adiabatic regime, the packet starting from $1\sigma_u$ stays in the ascending valley, which results in the slowdown of dissociative motion. In the diabatic regime, the packet localized in a valley moves on the descending and ascending valleys alternately: roughly speaking, the dissociative motion is no longer accelerated nor decelerated on the average. The dynamics on the 2D effective potential clearly shows that the correlation between the electronic and nuclear motions causes the slowdown of the dissociative motion.

To explain the slowdown of dissociation, one may also use the potentials E_1 and E_2 of the two phase-adiabatic states $|1\rangle$ and $|2\rangle$. The diagonal correction term $(\partial\theta/\partial R)^2/m_p$ in Eqs. (3.6) is negligible ($<3\times10^{-5}$). The molecule dissociates more slowly on the upward potential E_2 than on the field-free $1\sigma_u$ potential. To estimate kinetic energies of the fragments, in this paper, we just run classical trajectories on E_2 and E_1 using the semiclassical formalism by Thachuk *et al.*[43,53] They propose a criterion as to how classical trajectories should be hopped between time-dependent surfaces. The conservation principle to apply during a hop depends upon its physical origin. The nonadiabatic coupling $\partial\theta/\partial t$ mainly induces energy exchange between the electron and the field. When $\partial\theta/\partial t$ is dominant, nuclear momentum conservation is appropriate. On the other hand, when $v\partial\theta/\partial R$ is dominant, energy exchange occurs between the electron and nuclei: total energy conservation is appropriate. The two limiting cases can be smoothly bridged with a physically justified conservation scheme.[43]

Here we simply apply the rule of momentum conservation to hoppings at and after $t=2\pi/\omega$ (where $v\partial\theta/\partial R<0.02\partial\theta/\partial t$). The initial condition at $t=0$ is that the velocity of the nuclear motion on E_2 is zero at $R=2.12(\approx R_e)$, for which without the second pulse the kinetic energy of the fragments is the same as the quantum-mechanical average 4 eV. If, under the second pulse, the trajectory stays on E_2 until $t=2\pi/\omega$ and the case then switches to the diabatic regime, the kinetic energy of the fragments is reduced to 2.8 eV. [In the diabatic regime, the trajectory is assumed to hop between E_1 and $E_2(\approx-0.5\pm R|E(t)|/2)$ every half cycle.] It is reduced to 2.9 eV, if the packet stays on E_2 until $t=3\pi/\omega$. The values of reduced kinetic energy are close to the quantum-mechanical value in the 3D simulation, 3.2 eV. This is consistent with the fact that the line between the adiabatic and diabatic regimes can be drawn between $t=2\pi/\omega$ and $3\pi/\omega$ (as will be shown in Fig. 8).

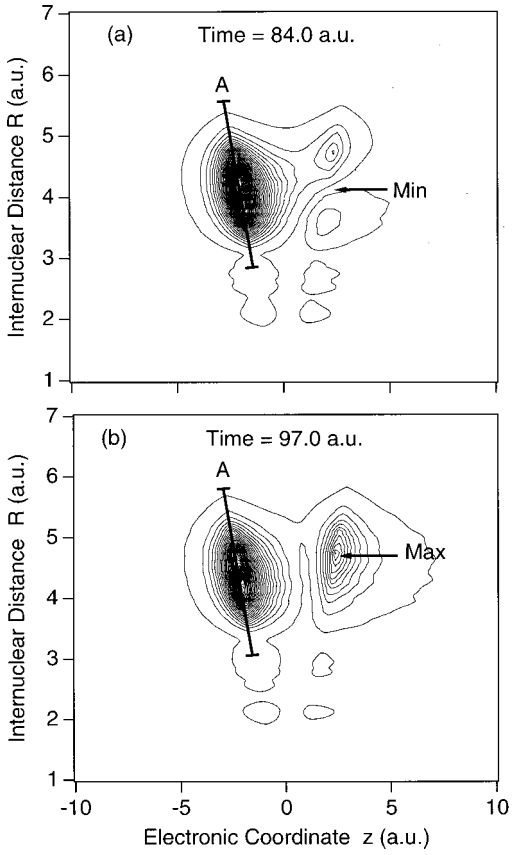

FIG. 7. Contour maps of $\int|\phi(\rho,z,R)|^2\rho d\rho$ at (a) $t=84.0$ and (b) $t=97.0$. The change in the population of the right well indicates that interwell electron transfer occurs within a half optical cycle.

D. Ultrafast electron transfer within a half optical cycle

Ultrafast interwell electron transfer results from a correlation between the electronic and nuclear motions. In Fig. 7, we show contour maps of the probability (4.3) at (a) $t=84$ and (b) $t=97$. In the second half cycle ($61<t<122$), the greater part of the density resides in the left (ascending) well; and this overall localization is in accordance with the adiabatic theorem. However, we note that the population in the right well is smaller at $t=84$ than at $t=97$, i.e., it changes drastically within a very short time. The distribution in the right well has a minimum (Min) in Fig. 7(a) and has a maximum (Max) in Fig. 7(b). These two types of wave function alternately appear with the period of ~24 in the second half optical cycle and the populations in the right and left wells oscillate accordingly.

The interwell electron transfer within a half cycle is explained using the two-state model. By solving the coupled Eqs. (3.6), we can estimate time-dependent populations as shown in Fig. 8. Here, the internuclear distance is treated as a time-dependent parameter $R(t)$. The quantum-mechanical average $\langle R(t)\rangle$ under the second pulse (solid line in Fig. 5) is used as $R(t)$. In the first half cycle $t\leqslant61$, the state is perfectly kept in $|2\rangle$. In the second half cycle, overall, the adiabatic picture still holds: P_L turns larger than P_R. However, we observe an oscillatory behavior in P_L and P_R. While the electronic distribution is completely localized to the left at $t\approx84$, it is delocalized to some extent at $t\approx96$ and it is once

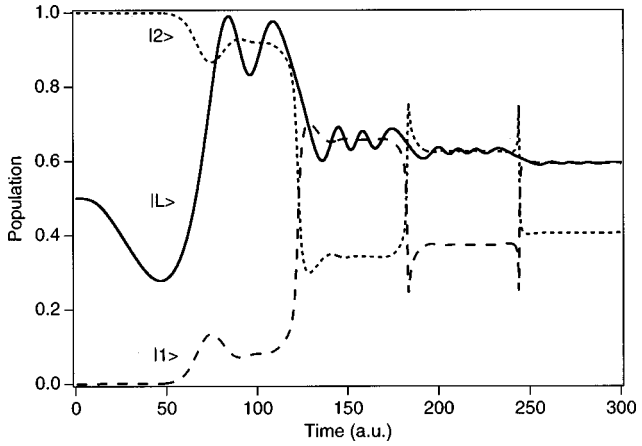

FIG. 8. Time-dependent populations in the two-state model. The solid line represents the population of the left well state $|L\rangle$. The dotted and broken lines denote the populations of the upper and lower phase-adiabatic states $|2\rangle$ and $|1\rangle$, respectively. The internuclear distance is replaced with its quantum-mechanical average in the 3D calculation (solid line in Fig. 5).

more delocalized at $t\approx 108$. This rapid oscillation period ~ 24 of the alternate appearances of localization and delocalization is almost the same as the one observed in the 3D simulation.

During any half cycle, as demonstrated in Fig. 8, the populations of $|1\rangle$ and $|2\rangle$ are nearly constant. Combining this fact with Eq. (3.6), we find that χ_j can be expressed as the product of the phase factor $\exp\{-i\int^t[E_j(R,t')+(\partial\theta/\partial R)^2/m_p]dt'\}$ and the modulus. At $t=96$, θ in Eqs. (3.8) is ≈ -0.66, which changes slowly in comparison with the rapid oscillation period ~ 24. The first two terms in Eqs. (3.8) are therefore not responsible for the rapid oscillation. It is the interference term in Eqs. (3.8) that is responsible for the rapid oscillation,

$$\cos 2\theta \chi_1^*(R)\chi_2(R) \propto \cos 2\theta |\chi_1^*(R)\chi_2(R)| \exp\left\{-i\int^t [E_2(R,t') - E_1(R,t')]dt'\right\}. \tag{4.5}$$

The period of the phase factor, $2\pi/[E_2(R,t)-E_1(R,t)]$ (~ 23 at $t=96$), corresponds to the difference between the points of localization at $t=84$ and $t=108$.

As known from Eqs. (3.8), if $\chi_1(R)=\chi_2(R)$, P_L/P_R is independent of R [for the above-mentioned treatment, $\chi_1(R)=\chi_2(R)=\delta(R-R(t))$]. This is not the case for the 3D simulation. As shown in Figs. 7, P_L/P_R depends on R. The shape of the section cut along the line A is nearly given by $|\chi_2(R)|^2$ and the right well populations for Figs. 7(a) and 7(b) can be expressed as $0.98|\chi_1(R)|^2+0.016|\chi_2(R)|^2 \mp 0.25|\chi_1^*(R)\chi_2(R)|$, respectively. The interference term is relatively large where $\chi_1(R)$ and $\chi_2(R)$ overlap with each other. The position of maximum overlap, e.g., Max in Fig. 7(b), is larger in R than the peak position in the left well (the peak of $|\chi_2(R)|^2$). This is a proof that χ_1 moves outward faster than χ_2. If momentum conservation is applied to the hop at $t=\pi/\omega$, the trajectory runs faster on E_2 than on E_1. The discrepancy means that energy exchange occurs between the electron and nuclei. The packet $|2\rangle|\chi_2\rangle$ prepared by the pump pulse splits, around $t=\pi/\omega$, into $|2\rangle|\chi_2\rangle$ and $|1\rangle|\chi_1\rangle$. At $t=\pi/\omega$, $\langle R\rangle=3.6$; the energy gap is $\Delta E_{ug}\approx 0.13$. Part of this electronic energy is converted to the nuclear motion on E_1 because $v\partial\theta/\partial R$ is as large as $0.1\partial\theta/\partial t$.

We conclude that the ultrafast electron transfer discussed above is due to the interference between $|1\rangle$ and $|2\rangle$ within a half cycle (not at crossing points). The interference disappears when $|\chi_1\rangle$ and $|\chi_2\rangle$ do not overlap with each other. The difference in motion between the two nuclear packets caused by electronic motion changes the pattern in ultrafast interwell electron transfer. If the second pulse is stronger (for instance, $\varepsilon_0=0.3$ and $\omega=0.07$), the interference term is larger and the oscillation in P_R becomes more pronounced. In the diabatic regime, θ is close to $\pi/4$ except for the vicinities of crossing points; consequently, the interference term in Eqs. (3.8) becomes negligible.

E. Dependence of ionization on the internuclear distance: Ionization from the ascending well

It has been reported that there are some ''critical'' internuclear distances at which ionization is enhanced. Dependence of the ionization on the internuclear distance R is attributed to the double-well nature of the effective electronic potential which leads to a different ionization mechanism from the atomic case.[23,24] As shown in Fig. 2, the key quantities for ionization are E_1, E_2, and the inner and outer barrier heights. The barrier heights are determined by the sum of Eqs. (2.2) and (2.3). As R increases, the outer barrier is more suppressed by the dipole interaction. The height V_0 decreases as $-2\sqrt{|E(t)|}-R|E(t)|/2$ at large R. On the other hand, the height of the inner barrier, V_1, increases as $-3/R$ in the small R region (say, $R<4$) and increases as $-2\sqrt{|E(t)|}+R|E(t)|/2$ at large R. The adiabatic energies E_1 and E_2 are nearly equal to E_g and E_u, respectively, for the small R region, and change as $0.5\mp R|E(t)|/2$ as R increases. In the large R region ($R>10$), the energy difference between E_1 and E_2 is nearly the same as that between the two barrier heights: the barrier suppression is atomlike.

Except in the large R region, the relative energy E_2-V_B is higher than E_1-V_o, where V_B is the maximum of V_o and V_I. The upper adiabatic state $|2\rangle$ is easier to ionize than $|1\rangle$. The relative energy E_2-V_B takes the maximum value at $R=R_x$, where R_x is the position where V_o and V_I are equal to each other; E_2-V_B is largest at $R\approx 4.2$ for $|E(t)|=0.096$ [it is peaked at $R\approx 5.2$ for $E(t)=0.06$ and at $R\approx 7.5$ for $E(t)=0.03$]. Ionization is thus expected to be enhanced when $|2\rangle$ is populated and R is near R_x. To embody this idea, we also solve the 2D time-dependent Schrödinger equation obtained by fixing R in Eq. (2.1). We discuss the ionization processes in R-fixed cases first, and then the ionization in the 3D simulation.

1. R-fixed cases

We present the results of two cases. In the first case (called case U), the molecule is assumed to be prepared in $1\sigma_u$ by a pump pulse. Then, the second pulse used in previous subsections, which induces ionization, is applied. Case U

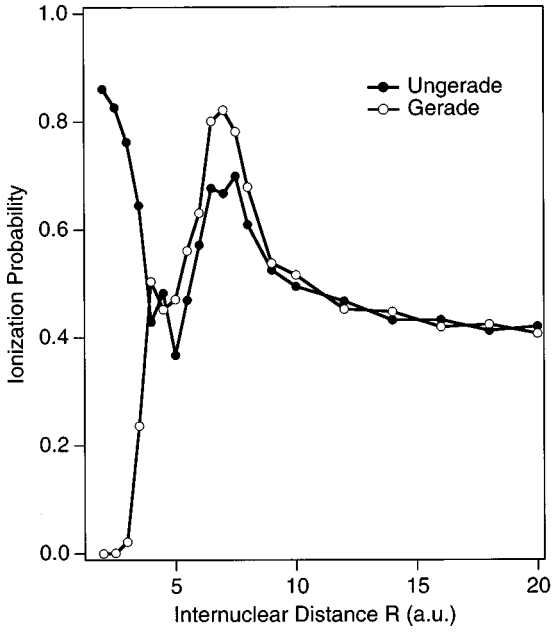

FIG. 9. Ionization probability of H_2^+ as a function of the internuclear distance. The parameters for the pulse are the same as those of the second pulse. The closed circles denote ionization probabilities in the case where the initial state at $t=0$ is $1\sigma_u$ (case U), and the open circles denote those for $1\sigma_g$ (case G).

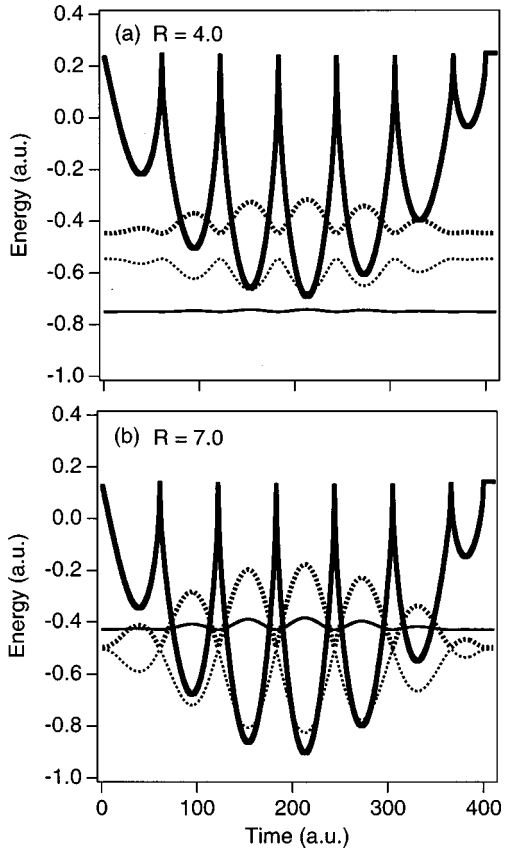

FIG. 10. Relation of E_1 and E_2 with the maxima of the inner and outer barriers. The applied field is the second pulse. The internuclear distance is fixed: (a) $R=4.0$ and (b) $R=7.0$. The outer barrier is designated by the bold–solid line and the inner barrier is designated by the thin–solid line. The barrier heights are defined for the instantaneous potential at $\rho=0$. The bold-dotted line denotes E_2 and the thin-dotted denotes E_1.

corresponds to the situation in the present 3D simulation. In the second case (case G), only the second pulse is applied to the molecule in $1\sigma_g$ (no pump pulse is applied). Most discussions of enhanced ionization in intense fields have been developed in case G. The ionization probabilities for the two cases are plotted in Fig. 9 as functions of R. The closed circles denote ionization probabilities for case U and the open circles denote those for case G. Critical internuclear distances are observed in both cases.

(i) Case U. In the small R region ($R<4$), the ionization probability increases with decreasing R. The small R region is characterized by its adiabaticity. Only the doorway state to ionization, namely $|2\rangle$, which is adiabatically connected with $1\sigma_u$, is populated (the flow into $|1\rangle$ becomes less and less with decreasing R). Since, as shown in Fig. 2(a), E_2 is much higher than the barriers, the probability of passing over the outer barrier is extremely high.

As R increases toward the intermediate region, the ionization probability decreases to the minimum at $R\sim4$; it increases again and has a peak at $R\sim7$. The mechanism of ionization can be clearly revealed by using analyses based on the two-state model. The maxima of the inner and outer barriers for $R=4$ and 7 are plotted in Fig. 10 against time, together with E_1 and E_2. Shown in Fig. 11 are the time-dependent populations of $|1\rangle$ and $|2\rangle$ obtained by mapping the 2D wave packet (the total population is less than unity because of the ionization). For $R=4$, ionization occurs mainly in the time domain between $t=2\pi/\omega$ and $t=3\pi/\omega$ (domain I); for $R=7$, ionization occurs also in the domain between $3\pi/\omega$ and $4\pi/\omega$ (domain II). The detailed explanation is given below.

For $R=4.0$, in domain I ($122<t<183$), E_2 is higher than the barriers and the population of the state $|2\rangle$($P_2\approx0.7$) overweighs that of $|1\rangle$($P_1\approx0.3$). As shown in Fig. 12(a), the total population P_1+P_2 is reduced from ~0.91 to ~0.65, which corresponds to the reduction in P_2 denoted by the open circles in Fig. 11(a). This reduction is a clear proof of ionization from $|2\rangle$, because without ionization the population P_2 is nearly constant between the level crossings at $t=2\pi/\omega$ and $t=3\pi/\omega$. Around $t=3\pi/\omega$, however, complete exchange of P_2 with P_1 takes places because the field envelope is coming close to the peak ($\delta\ll1$):P_2 is reduced to ~0.1. In domain II ($183<t<244$), although E_2 is much higher than the barriers, the reduction in P_1+P_2 is only a little (~0.05) because of the low population of $|2\rangle$.

For $R=7.0$, P_2 is ~0.45 at the entrances to the two time domains and the energy E_2 is higher than the barriers in both time domains. It should be noted in Fig. 11(b) that P_2 is recovered from ~0.23 to ~0.44 by the nonadiabatic transition around $t=3\pi/\omega$. The total population P_1+P_2 thus decreases in both time domains. The corresponding reductions in P_2 are denoted in Fig. 11(b) by the open marks. As expected, the ionization probability is a decreasing function of R in the region of $R>7$, and converges to the value 0.42 which is the same as that of the H atom.

In short, the criterion for enhanced ionization is as follows: whenever P_2 is large and the barriers are low enough for the electron to tunnel from the ascending well, ionization

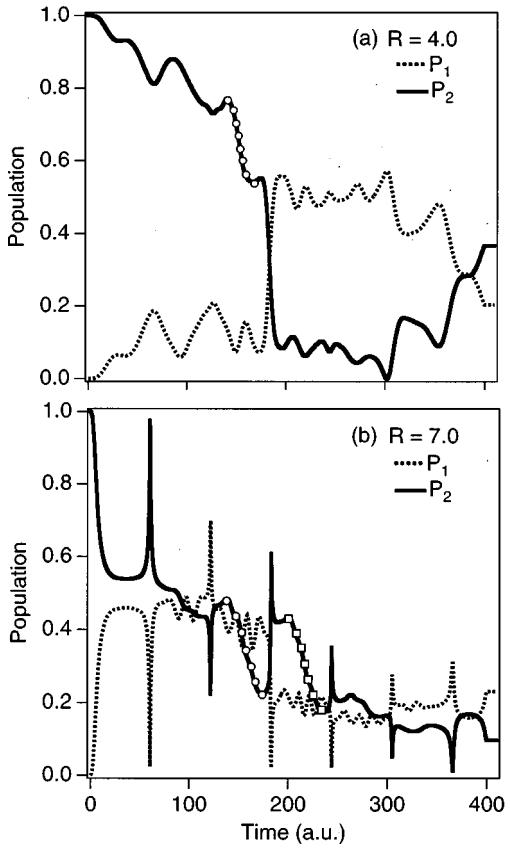

FIG. 11. Populations obtained by mapping the R-fixed 2D packet onto the phase-adiabatic states $|1\rangle$ and $|2\rangle$: (a) $R=4$ and (b) $R=7$ (case U). The dotted line denotes the population of $|1\rangle$ and the solid line denotes that of $|2\rangle$. Because of ionization, the population of $|2\rangle$ significantly decreases in two time domains. The reduction in domain I is denoted by the circles and the reduction in domain II is denoted by the squares.

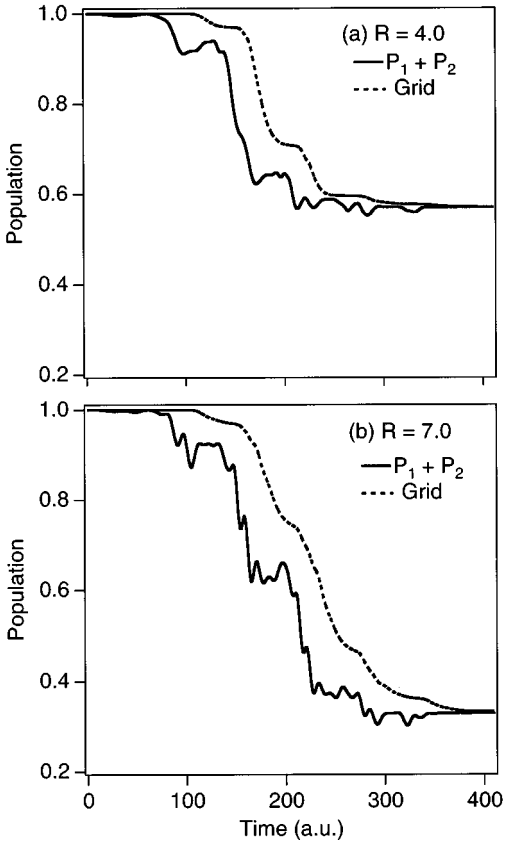

FIG. 12. Populations of the 2D packet for (a) $R=4$ and (b) $R=7$. The solid line denotes the total population of the two phase-adiabatic states and the dotted line denotes the population remaining in the whole grid range.

is enhanced. Figure 12 also demonstrates that the population remaining within the whole grid range is identical with the total population P_1+P_2 after a long lapse of time. All the intermediates in the other states are eventually ionized. This rule is valid also for all the cases discussed below.

(ii) Case G. As in case U, the dependence of the ionization probability on R is fully analyzed by mapping the wave function onto the two adiabatic states. The above criterion for enhanced ionization is also valid for this case. At $R \approx 2.0$, the ionization probability is almost zero: the state $|2\rangle$ is hardly populated from $|1\rangle$. As R approaches zero, the system is regarded as the He^+ atom of large ionization potential $I_p=2$. As R increases to intermediate internuclear distances, the ionization probability rapidly increases. In the intermediate R region, the ionization probability exceeds that of the H atom by a factor of two, although the ionization potential I_p is always larger than that of H. This is due to a combined effect of efficient barrier suppression and nonadiabatic transitions to $|2\rangle$. As R increases, the difference between cases U and G becomes smaller because of nonadiabatic transitions.

2. The 3D simulation

The two-state model is also useful in analyzing the ionization process of the 3D simulation in which nuclear motion is considered quantum mechanically. The population remaining in the 3D whole grid range is shown in Fig. 13. The ionization probability is 0.71, which is a little higher than the peak around $R=7$ in case U. The first four sharp drops in the population up to $t \approx 300$ indicate that ionization is enhanced

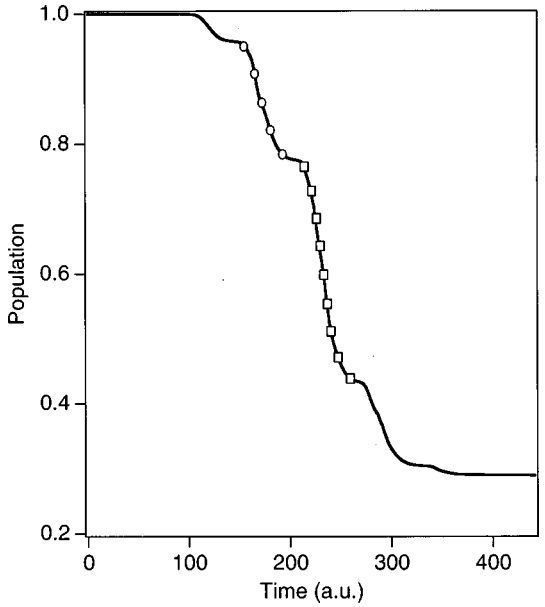

FIG. 13. Population in the whole grid range for the 3D simulation. The circles and the squares denote domains I and II, respectively.

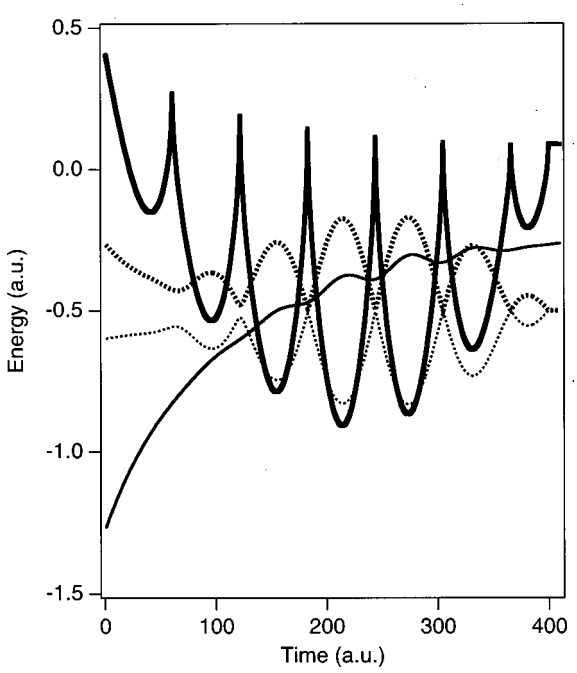

FIG. 14. Relation of E_1 and E_2 with the inner and outer barriers in the 3D simulation. The notations are the same as in Fig. 10. The internuclear distance is replaced with its quantum-mechanical average (solid line in Fig. 5).

four times. The maxima of the inner and outer barriers are shown in Fig. 14, together with E_1 and E_2. In this calculation, the internuclear distance R is treated parametrically to be replaced with the quantum-mechanical average $\langle R(t)\rangle$ for the 3D simulation (solid line in Fig. 5). As known from Fig. 14, E_2 goes beyond the barriers four times between $t=85$ and 295, which is consistent with the first four drops in Fig. 13.

Although, as shown in Fig. 14, the degree of barrier suppression, E_2-V_B, is a little larger in domain I than in domain II, the reduction in population is more pronounced in domain II. The enhancement of ionization in domain II comes from the large population of $|2\rangle$. Although ionization is ignored in Fig. 8, we presume that the incoming P_2 is $\sim$0.3 in domain I and $\sim$0.65 in domain II. Nearly complete exchange of the populations of $|1\rangle$ and $|2\rangle$ at $t=3\pi/\omega$ shown in Fig. 8 suggests that the incoming P_2 in domain II is close to P_1 in domain I. Thus, whenever P_2 is large and the barriers are low enough for tunneling, ionization is enhanced irrespective of the nuclear motion.

If R is replaced with $\langle R(t)\rangle$, the ionization probability is 0.72, which is nearly equal to the value 0.71 in the 3D simulation. As suggested by the R-dependence of the ionization probability in Fig. 9, the condition of nonadiabatic transitions and the aspect of barrier suppression change with R. Considering that the full width at half maximum of the present packet is as large as $\sim$1 in R, the coincidence in ionization probability is probably attributed to the fact that the ionization occurs mainly in domain II, i.e., in the region $6.5<R<7.5$. The R-dependence of the ionization probability thereabouts is not as strong as in the small R region (cf. Fig. 9). For instance, the ionization probabilities for two trajectories $R(t)=\langle R(t)\rangle\pm0.5$ with the same speed are 0.69 and 0.71, respectively. In the present case, the packet width in R does not affect the ionization probability severely. The packet width in R leads to a distribution of trajectories $R(t)$ around $\langle R(t)\rangle$. The average over ionization probabilities for different $R(t)$ is closer to the ionization probability 0.71 for the 3D simulation.

We also calculate the ionization probability for the quantum-mechanical average $\langle R(t)\rangle_{NS}$ obtained when the second pulse is not applied (broken line in Fig. 5). In this case, the ionization probability is 0.68, which is smaller than the value 0.72 for $\langle R(t)\rangle$ (the difference converges to 0.05 with increasing grid size). The population of $|2\rangle$ for $\langle R(t)\rangle_{NS}$ is nearly identical with that for $\langle R(t)\rangle$ shown in Fig. 8. The difference between $\langle R(t)\rangle_{NS}$ and $\langle R(t)\rangle$ is $\sim$0.3 even in domain II of dominant ionization. The corresponding difference in E_2-V_B is less than 0.01, which is not large enough to reproduce the difference in ionization probability.

To fully explain the difference, we propose to consider an additional effect, namely, the finite speed of the nuclei. Suppose that the electric field is positive and is strong enough for the electron density in $|2\rangle$ to be one-sided to the ascending well (in this case, right well). Because of the dissociative motion, the right nucleus proceeds rightward. If the electron cannot follow the fast nuclear motion tight (imagine in Fig. 6 a motion from B parallel to the R-axis), the lagging electron is pulled by the right nucleus. This force is opposite to the direction of ionization. The slowdown of dissociative motion on E_2 allows the tight following and can therefore help the ionization probability to increase.

V. SUMMARY AND CONCLUSIONS

We have performed full dynamical calculations for a realistic 3D model of H_2^+ by solving the time-dependent Schrödinger equation for the system. Although the nuclear motion is restricted to the polarization direction z of the laser electric field, the electron moves in three-dimensional space. To study electronic and nuclear correlation dynamics in intense laser fields, we have coped with awkward Coulomb potentials without introducing any approximations such as the B-O separation of electronic and nuclear degrees of freedom. The success is attributed to the introduction of a generalized cylindrical coordinate system.

The response to a laser electric field of H_2^+ is classified into two regimes. In the adiabatic regime, electron density transfers from a well associated with a nucleus to the other well every half optical cycle; in the diabatic regime, interwell electron transfer is suppressed. As the field intensity and the internuclear distance R increase, interwell transition is further suppressed. As the 3D packet pumped onto $1\sigma_u$ moves toward larger internuclear distances, apart from the ionized component, the electron density is locked in each well. The electron distribution can be asymmetric between the two wells if the pulse length is as short as the present one. One may be able to adjust the pulse shape and the frequency so that the electron density is eventually localized in a well.

The correlation between the electronic and nuclear motions accelerates or decelerates the dissociative motion of

$H+H^+$. The acceleration and deceleration of dissociative motion in intense fields are interpreted using the time-dependent ''effective'' 2D potential surface obtained by fixing the transverse electronic coordinate ρ in the total potential. The ''effective'' 2D potential has an ascending and a descending valley along $z=\pm R/2$ which change places with each other every half cycle. In the adiabatic regime, the packet pumped onto $1\sigma_u$ stays in the ascending valley, which results in the slowdown of dissociative motion. In the diabatic regime, the packet localized in a valley gains almost no extra kinetic energy because it moves on the descending and ascending valleys alternatively. Correlation between the dissociative motion and the interwell electron transfer can be clearly visualized on the ''effective'' 2D potential. Characteristic features of nuclear motion are also reproduced in terms of the potential surfaces E_1 and E_2 of the two phase-adiabatic states $|1\rangle$ and $|2\rangle$. The lower state $|1\rangle$ is localized in the descending valley and $|2\rangle$ is in the ascending valley. The kinetic energy distribution of fragments for the channel $H+H^+$ can be roughly estimated just by combining the coupled equations for the two phase-adiabatic states with a classical or quantal treatment of nuclear motion. The average kinetic energy of the fragments estimated by running classical trajectories on $E_2(R,t)$ is consistent with that in the 3D simulation.

In the intermediate regime, both $|1\rangle$ and $|2\rangle$ are populated because of nonadiabatic transitions. The interference between them occurs not only at level crossing points but also within a half cycle (not at crossing points). The latter type of interference results in ultrafast interwell electron transfer with the period $2\pi/(E_2-E_1)$. In intense fields, the period can be much shorter than a half cycle. The interference pattern due to ultrafast interwell electron transfer reflects the fact that the nuclear packet $|\chi_1|$ associated with $|1\rangle$ moves toward larger R faster than $|\chi_2\rangle$. Such interference disappears when $|\chi_1\rangle$ and $|\chi_2\rangle$ do not overlap with each other (e.g., if the speeds of $|\chi_1\rangle$ and $|\chi_2\rangle$ are extremely different from each other).

Using the R-fixed 2D model of H_2^+, we have also examined how ionization is enhanced at specific internuclear distances. Analyses are made by mapping the 2D packet onto $|1\rangle$ and $|2\rangle$. While the electric field is near a local maximum or minimum, the population P_2 of $|2\rangle$ decreases but P_1 is nearly constant. This type of reduction in P_2 is direct evidence of ionization from the upper adiabatic state $|2\rangle$ (roughly speaking, from the ascending well). Ionization is enhanced whenever P_2 is large and the barriers are low enough for the electron to tunnel from the ascending well. The criterion is also valid for the ionization process in the present 3D simulation. The width in R of the packet pumped onto $1\sigma_u$ does not affect the ionization probability severely. On the other hand, the packet's speed affects the ionization. The lag of the electronic motion with respect to the nuclear motion can reduce the ionization probability. The slowdown of dissociative motion induced by the laser field has therefore two effects on the ionization process: the longer residence time in the critical range of enhanced ionization and the nearly perfect following of the electronic motion to the speed of the nuclei.

It is worth noting that all the intermediates in other adiabatic states than $|1\rangle$ and $|2\rangle$ are eventually ionized irrespective of the nuclear motion. After a long lapse of time, the population within the whole grid range is identical to the total population P_1+P_2. This gives us a definite rule as to how many phase-adiabatic states should be contained in the analysis of the ionization process. The final population within the whole grid range must be identical to the total population of the chosen phase-adiabatic states. We are constructing a minimum set of phase-adiabatic states for a one-dimensional model of H_2 to investigate ionization processes in the two-electron molecule.[54]

ACKNOWLEDGMENTS

We would like to thank Professor A. D. Bandrauk, Professor S. L. Chin, Dr. S. Chelkowski, and Dr. Y. Ohtsuki for helpful discussions. This work was supported in part by the Department of High-Density Optical Pulse Generation and Advanced Material Control Techniques and also by a Grant-in-Aid for Scientific Research from the Ministry of Education, Science and Culture, Japan (09894016).

APPENDIX: TIME EVOLUTION WITH THE D'YAKONOV SCHEME

If the time step Δt is sufficiently small, the short time propagator $\exp[-iH\Delta t]$ can be replaced with an approximate propagator that is accurate up to a certain order of Δt. The wave function at the desired time is obtained by operating such an approximate propagator on the wave function iteratively. We have tested various approximate propagators to see which one is the best for the 1D attractive Coulomb potential. The following approximate propagator called the Cayley form is found to be the most efficient one;[35]

$$e^{-iH\Delta t}\approx\frac{1-iH\Delta t/2}{1+iH\Delta t/2}. \tag{A1}$$

Using the Cayley form, the wave function at time $t_n=n\Delta t+t_0\psi^n$, can be advanced by solving the equation $(1+iH\Delta t/2)\psi^{n+1}=(1-iH\Delta t/2)\psi^n$ (this implicit scheme is called the Crank–Nicholson one[55]). The differential operators are usually evaluated by the finite difference method. The resultant band diagonal system of linear algebraic equations, which is pentadiagonal for the five-point finite difference method, can be solved efficiently by using LU decomposition.

Although the Cayley–Crank–Nicholson (CCN) scheme has many advantages, such as the conservation of energy, its direct application has been limited only to one- or two-dimensional problems.[56] It has, however, been known that the inefficiency of computation for multidimensional cases is cured by a different way of generalizing the CCN scheme, namely, the alternating-direction implicit method (ADI). For the ADI, the system of equations to be solved can be reduced to band diagonal systems for one-dimensional spaces, and the quality of the CCN is maintained.

In the following, we briefly review a 3D version of the ADI. The ADI embodies the powerful idea of operator split-

ting and time splitting. For instance, by using the ADI one can split the time evolution operator $\exp[-i(A+B+C)\Delta t]$ as

$$e^{-i(A+B+C)\Delta t} \approx \frac{1}{1+iC\Delta t/2}\frac{1}{1+iB\Delta t/2} \times \frac{1-iA\Delta t/2}{1+iA\Delta t/2}(1-iB\Delta t/2)(1-iC\Delta t/2). \tag{A2}$$

where A, B, and C are arbitrary operators. The operation is separated into three steps by introducing ''artificial'' intermediate states $\psi^{n+1/3}$ and $\psi^{n+2/3}$,

$$(1+iA\Delta t/2)\psi^{n+1/3} = (1-iA\Delta t/2)(1-iB\Delta t/2) \times (1-iC\Delta t/2)\psi^{n}, \tag{A3a}$$

$$(1+iB\Delta t/2)\psi^{n+2/3} = \psi^{n+1/3}, \tag{A3b}$$

$$(1+iC\Delta t/2)\psi^{n+1} = \psi^{n+2/3}, \tag{A3c}$$

which is known as the D'yakonov scheme.[40] For time-dependent Hamiltonians, to keep the accuracy of order Δt^2, A, B, and C in Eqs. (A3) must be replaced with those at the midpoint of the time step, $t_{n+1/2}=t_n+\Delta t/2$.

For the 3D problem to be reduced to three sets of one-dimensional problems, the differential operators involved in A, B, and C must be those of different freedoms. For H_2^+, the three kinetic energy parts K_R, K_ξ, and K_ζ in the Hamiltonian Eq. (2.9) are confined in A, B, and C separately. We furthermore divide the three-body Coulomb interactions V into nucleus–nucleus interaction $1/R$ and nucleus–electron interaction $V_1(\rho,z,R)=V(\rho,z,R)-1/R$. The most reasonable way of separation is as follows:

$$A = K_R + \frac{1}{R}, \tag{A4a}$$

$$B = K_\xi + \frac{1}{2}V_1(\rho,z,R) + \frac{m^2}{2\rho^2}, \tag{A4b}$$

$$C = K_\zeta + \frac{1}{2}V_1(\rho,z,R) + V_E(z,t). \tag{A4c}$$

[1] *Atoms in Strong Laser Fields*, edited by C. A. Nicolaides, C. W. Clark, and M. H. Nayfeh, NATO ASI Series B (Plenum New York, 1990), Vol. 212.
[2] J. Javanainen, J. H. Eberly, and Qichang Su, Phys. Rev. A **38**, 3430 (1988).
[3] P. B. Corkum, N. H. Burnett, and F. Brunel, Phys. Rev. Lett. **62**, 1259 (1989).
[4] J. H. Eberly, J. Japanainen, and K. Rzazewski, Phys. Rep. **204**, 331 (1991).
[5] M. Lewenstein, K. C. Kulander, K. J. Schafer, and P. H. Bucksbaum, Phys. Rev. A **51**, 1495 (1995).
[6] K. Burnett, V. C. Reed, J. Cooper, and P. L. Knight, Phys. Rev. A **45**, 3347 (1992).
[7] J. L. Krause, K. J. Schafer, and K. C. Kulander, Phys. Rev. A **45**, 4998 (1992).
[8] K. J. Schafer and K. C. Kulander, Phys. Rev. A **45**, 8026 (1992).
[9] T. Zuo, A. D. Bandrauk, M. Ivanov, and P. B. Corkum, Phys. Rev. A **51**, 3991 (1995).
[10] P. Moreno, L. Plaja, V. Malyshev, and L. Roso, Phys. Rev. A **51**, 4746 (1995).
[11] I. Zhou, J. Peatross, M. M. Murnane, and H. C. Kapteyn, Phys. Rev. Lett. **76**, 752 (1996).
[12] I. P. Christov, J. Zhou, J. Peatross, A. Rundquist, M. M. Murnane, and H. C. Kapteyn, Phys. Rev. Lett. **77**, 1743 (1996).
[13] P. B. Corkum, Phys. Rev. Lett. **71**, 1994 (1993).
[14] L. V. Keldysh, Sov. Phys. JETP **20**, 1307 (1965).
[15] F. H. M. Faisal, J. Phys. B **6**, L89 (1973).
[16] H. R. Reiss, Phys. Rev. A **22**, 1786 (1980).
[17] S. Augst, D. D. Meyerhofer, D. Strickland, and S. L. Chin, J. Opt. Soc. Am. B **8**, 858 (1991).
[18] M. V. Ammosov, N. B. Delone, and V. P. Krainov, Sov. Phys. JETP **64**, 1191 (1986).
[19] C. Cornaggia, J. Lavancier, D. Normand, J. Morellec, P. Agostini, J. P. Chambaret, and A. Antnetti, Phys. Rev. A **44**, 4499 (1991).
[20] C. Cornaggia, D. Normand, and J. Morellec, J. Phys. B **25**, L415 (1992).
[21] L. J. Fransinski, P. A. Hatherly, K. Codling, M. Larsson, A. Persson, and C.-G. Wahlstrom, J. Phys. B **27**, L109 (1994).
[22] P. A. Hatherly, M. Stankiewicz, K. Codling, L. J. Frasinski, and G. M. Cross, J. Phys. B **27**, 2993 (1994).
[23] T. Zuo and A. D. Bandrauk, Phys. Rev. A **52**, R2511 (1995).
[24] S. Chelkowski, T. Zuo, O. Atabek, and A. D. Bandrauk, Phys. Rev. A **52**, 2977 (1995).
[25] A. D. Bandrauk, Comments At. Mol. Phys. (to be published).
[26] T. Seideman, M. Yu. Ivanov, and P. B. Corkum, Phys. Rev. Lett. **75**, 2819 (1995); M. Ivanov, T. Seideman, and P. Corkum, Phys. Rev. A **54**, 1541 (1996).
[27] D. M. Villeneuve, M. Yu. Ivanov, and P. B. Corkum, Phys. Rev. A **54**, 736 (1996).
[28] *Molecules in Laser Fields* edited by A. D. Bandrauk (Marcel Dekker, New York, 1994).
[29] A. Giusti-Suzor, F. H. Mies, L. F. DiMauro, E. Charron, and B. Yang, J. Phys. B **28**, 309 (1995).
[30] T. F. George, I. H. Zimmerman, J. M. Yuan, J. R. Laing, and P. L. Devries, Acc. Chem. Res. **10**, 449 (1977).
[31] T. T. Nguyen-Dang and D. Bandrauk, J. Chem. Phys. **79**, 3256 (1983).
[32] B. Sheehy and L. F. DiMauro, Annu. Rev. Phys. Chem. **47**, 463 (1996).
[33] K. C. Kulander, F. H. Mies, and K. J. Schafer, Phys. Rev. A **53**, 2562 (1996).
[34] I. Kawata, H. Kono, and Y. Fujimura, Chem. Phys. Lett. **289**, 546 (1998).
[35] H. Kono, A. Kita, Y. Ohtsuki, and Y. Fujimura, J. Comput. Phys. **130**, 148 (1997).
[36] J. R. Hiskes, Phys. Rev. **122**, 1207 (1961).
[37] C. Froese Fischer, *The Hartree-Fock Method for Atoms* (Wiley, New York, 1976), p. 223.
[38] F. Gygi and G. Galli, Phys. Rev. B **52**, R2229 (1995); F. Gygi, *ibid.* **51**, 11190 (1995).
[39] E. Fattal, R. Baer, R. Kosloff, and D. Kosloff, Phys. Rev. E **53**, 1217 (1996).
[40] See, for example, A. R. Mitchell, *Computational Methods in Partial Differential Equations* (Wiley, New York, 1969).
[41] F. H. Mies, A. Giusti-Suzor, K. C. Kulander, and K. J. Schafer in *Super-Intense Laser-Atom Physics*, edited by B. Piraux, A. L'Huillier, and K. Rzazewski, NATO ASI Series B (Plenum, New York, 1993), Vol. 316.
[42] R. S. Mulliken, J. Chem. Phys. **7**, 20 (1939).
[43] M. Thachuk, M. Yu. Ivanov, and D. M. Wardlaw, J. Chem. Phys. **105**, 4094 (1995); **109**, 5747 (1998).
[44] Y. Kayanuma, Phys. Rev. B **47**, 9940 (1993); Phys. Rev. A **50**, 843 (1994).
[45] Y. Teranishi and H. Nakamura, J. Chem. Phys. **107**, 1904 (1997); C. Zhu and H. Nakamura, *ibid.* **107**, 7839 (1997), and references therein.
[46] C. Zener, Proc. R. Soc. London, Ser. A **137**, 696 (1984).
[47] M. D. Feit, J. A. Fleck, Jr., and A. Steiger, J. Comput. Phys. **47**, 412 (1982); M. D. Feit and J. A. Fleck, Jr., J. Chem. Phys. **78**, 301 (1983).
[48] R. Kosloff and D. Kosloff, J. Comput. Phys. **63**, 363 (1986).
[49] The range where the adiabatic theorem is applicable is given, e.g., in A. Messiah, *Quantum Mechanics* (North-Holland, Amsterdam, 1970), Vol. 2, Ch. 17.
[50] J. M. Gomez Llorente and J. Plata, Phys. Rev. A **45**, R6958 (1992); M. Ivanov, P. Corkum, and P. Dietrich, Laser Phys. **3**, 375 (1993); Y. Dakhnovskii and R. Bavli, Phys. Rev. B **48**, 11020 (1993).
[51] F. Grossmann, T. Dittrich, P. Jung, and P. Hänngi, Phys. Rev. Lett. **67**, 516 (1991).
[52] F. Grossmann, T. Dittrich, P. Jung, and P. Hänngi, Z. Phys. B **84**, 315 (1991).
[53] P. Dietrich, M. Yu. Ivanov, F. A. Ilkov, and P. B. Corkum, Phys. Rev. Lett. **77**, 4150 (1996).
[54] H. Yu, T. Zuo, and A. D. Bandrauk, Phys. Rev. A **54**, 3290 (1996).
[55] A. Askar and A. S. Cakmak, J. Chem. Phys. **68**, 2794 (1978).
[56] E. A. McCullogh and R. E. Wyatt, J. Chem. Phys. **54**, 3592 (1971).